RSC Advances

PAPER

View Article Online
View Journal | View Issue

Cite this: *RSC Adv.*, 2025, **15**, 27279

Synthesis of magnetized ZIF-8 and Ag_2O nanocomposites as colloids for a designed magnetic column reactor for water treatment and enhanced removal of *Escherichia coli*

Mehrdad Zolfalizadeh,[a] Hadi Khalilnezhad,[b] Saeid Nickabadi[b] and Behrang Golmohammadi *[c]

Magnetic nanocomposite (MNC) colloids can be employed in guided systems under a magnetic field, as demonstrated in this work for the removal of *Escherichia coli* (*E. coli*) from water. Herein, we employed a magnetic reactor system incorporating an Fe_3O_4@ZIF-8@Ag_2O nanocomposite colloid with destructive power against bacteria, focusing on elucidating the influence of key parameters, including the applied magnetic field and the presence of the MNCs, on the efficiency of bacterial removal. To assess bacterial viability, experiments were conducted in both phosphate-buffered saline (PBS) and a standard aqueous solution. The experimental design aimed to optimize bacterial removal by employing a 2 mT magnetic field, generated by a solenoid coil-assisted tubular reactor, which contributed to the stabilization of the magnetic nanoparticle (MNP) colloids. As the bacterial suspension traversed the reactor, interactions between *E. coli* and the nanoparticles resulted in collisions that induced cellular disruption and subsequent cell death. Under magnetic field conditions, the removal efficiency of *E. coli* increased by 29.6% after 60 minutes relative to control experiments without a magnetic field, culminating in an overall removal rate of 99.83% within the same period. Additionally, kinetic modeling using the Weibull function in the absence of a magnetic field yielded a minimal root mean square error (RMSE) of 7%, while the maximum standard deviation in the average *E. coli* concentration reached 75% at 40 minutes under magnetic conditions. These findings suggest that using stable MNC colloids under a controlled magnetic field markedly improves bacterial removal from water.

Received 10th April 2025
Accepted 15th June 2025

DOI: 10.1039/d5ra02521d

rsc.li/rsc-advances

1. Introduction

Environmental pollution is a critical global challenge encompassing air, water, soil, and thermal contaminants. Water is an essential resource, and its quality is increasingly threatened by both domestic and industrial activities.[1] As freshwater resources diminish and wastewater production escalates, effective treatment becomes imperative to prevent the contamination of natural water bodies and reduce associated health risks.[2] Seawater contains significant amounts of dissolved minerals and supplements that could be considered a secondary source of raw materials.[3–6] Seawater is affected by a variety of pollutants, including plastics, industrial waste, sewage, and pathogenic microorganisms, such as *E. coli*, which should be treated as fast as possible, for instance, in water production on cruise ships or other naval vessels.[7,8] Different membrane technologies coupled with other technologies have been developed to address these challenges.[7,8] However, fast bacterial treatment of seawater remains an essential challenge on naval vessels.

Magnetic colloidal nanocomposite systems have recently emerged as a promising solution for antibacterial applications.[9–11] In this respect, Lin *et al.* demonstrated complete arsenic adsorption within 30 minutes using magnetic γ-Fe_2O_3 nanoparticles, with the adsorption process remaining stable across a pH range of 3 to 11 and unaffected by common anions.[12] Han *et al.* reported that manganese oxide-coated zeolite (MOCZ) effectively removed copper(II) and lead(II) ions from aqueous solutions, exhibiting a stronger affinity for lead.[13] Furthermore, Gonzalez-Vazquez *et al.* found that the application of an external magnetic field enhanced the removal rates of cadmium and zinc from activated carbon adsorbents.[14] In microbial decontamination, water treatment plants have adopted methods such as membrane filtration, powdered activated carbon adsorption, sand filtration, and oxidation to eliminate *E. coli*.[15–18] Complementary research has shown that

[a]*Faculty of Chemical and Petroleum Engineering, University of Tabriz, Tabriz, Iran*
[b]*Department of Mechanic Engineering, Imam Khomeini University of Marine Science & Technology, Nowshahr, Iran*
[c]*Department of Physical Chemistry, University of Tabriz, Tabriz, Iran. E-mail: behrangrose@gmail.com*

advanced materials, including $AgNO_3$-activated carbon composites and MNCs, offer substantial antibacterial activity, achieving removal efficiencies as high as 99.99% and enabling rapid disinfection at optimal concentrations.[19–22]

Auxiliary devices such as solenoid wire coils, which generate magnetic fields upon the passage of an electric current, have been employed to further enhance nanoparticle performance in water treatment systems.[23] Magnetic fields not only influence the migration and distribution of nanoparticles, as demonstrated in studies on water/alumina nanofluids,[24] but also improve the removal efficiency of contaminants in wastewater treatment processes, including the elimination of nitrogenous compounds and *E. coli*.[25–27] Collectively, these studies illustrate an integrated approach that combines advanced materials with magnetic field applications to achieve more effective and rapid water purification, addressing both chemical and microbiological contaminants while supporting environmental and public health objectives.

In this study, an advanced column reactor system filled with MNC colloid has been developed for water disinfection, and was designed to improve the bacterial removal efficiency from aqueous media. This system incorporates Fe_3O_4@ZIF-8@Ag_2O MNCs, which have demonstrated high removal efficiency even at low concentrations in a colloidal mixture of aqueous feed. There are, however, a few risks from the release of silver nanoparticles (AgNPs) into the environment. In essence, the increasing use of AgNPs across various consumer, industrial, and even agricultural sectors presents a tangible risk of environmental pollution. These nanoparticles can enter the environment through diverse pathways, including wastewater discharge, product disposal, and atmospheric deposition. Once in the environment, AgNPs pose a threat to a wide range of organisms, from aquatic life and soil microorganisms to potentially higher trophic levels through bioaccumulation. Their toxicity and the possibility of transformation into different, potentially harmful forms raise concerns about ecosystem disruption and long-term ecological consequences. Furthermore, the widespread release of these antibacterial agents could contribute to the growing problem of antibiotic resistance. While the full extent of their environmental impact is still under investigation, the presence of AgNPs in various environmental samples serves as a clear indicator of existing pollution. Therefore, continued research into their fate and effects, along with the development of strategies to minimize their release, is crucial to mitigate the potential environmental risks associated with the increasing use of AgNPs.[28–35]

The system was engineered to stabilize MNPs within the reactor, facilitating increased Brownian motion and enhancing interactions between nanoparticles and bacteria. We hypothesized that a magnetic field generated by a copper solenoid coil and supplied with direct current (DC) would stabilize the nanoparticles within the system and direct their movement along the coil's axis to isolate the effects of MNPs. The solenoid coil was specifically designed to minimize heat generation when a magnetic field was applied, which could reduce the *E. coli* removal. One advantage of this study over previous research in this field is the use of a novel antimicrobial nanostructure, guided by a new magnetic system, to enhance microbial removal efficiency.

2. Materials and methods

All analytical grade chemicals were purchased from Merck and used without further purification; these include silver nitrate ($AgNO_3$), sodium hydroxide (NaOH), sodium sulfite (Na_2SO_3), iron(III) chloride hexahydrate ($FeCl_3 \cdot 6H_2O$), zinc nitrate hexahydrate ($Zn(NO_3)_2 \cdot 6H_2O$), and 2-methylimidazole ($C_4H_6N_2$).

2.1. Preparation of nanocomposite

2.1.1. Synthesis of Fe_3O_4 nanoparticles. The synthesis method described by Wu *et al.* was followed.[36] In the initial step, 0.1 g of Na_2SO_3 and 1.4 g of $FeCl_3 \cdot 6H_2O$ were simultaneously added to 200 mL of distilled water, and the resulting solution was stirred at 25 °C for 1 hour under a nitrogen atmosphere. Subsequently, 1 mL of aqueous NaOH was added dropwise to the solution. After stirring for 5 minutes, the synthesized black Fe_3O_4 powder, serving as MNPs, was collected using a magnet, washed three times with deionized water and ethanol, and subsequently dried in an oven at 60 °C for 12 hours.

2.1.2. Synthesis of Ag_2O nanoparticles. A solution containing 3.05 g of $AgNO_3$ in 24 mL of distilled water was prepared by stirring at 500 rpm at 25 °C for 1 hour using a magnetic stirrer to ensure the complete dissolution and dispersion of the solute. Subsequently, 0.32 g of NaOH was added dropwise to the stirred solution to obtain pH = 14 under an argon atmosphere with continuous stirring for 1 hour. A brown precipitate was observed, indicative of the formation of silver oxide (Ag_2O).[37] The Ag_2O nanoparticles were allowed to sediment, after which they were separated from the solution and washed with distilled water and ethanol to remove impurities. The obtained nanoscale Ag_2O was dried in an oven at 80 °C for 12 hours.

2.1.3. Synthesis of ZIF-8. ZIF-8 nanocrystals were prepared *via* rapid precipitation in an aqueous medium following the protocol reported by Pan *et al.*[38] For solution A, 0.234 g of $Zn(NO_3)_2 \cdot 6H_2O$ was dissolved in 1.5 mL of distilled water, and for solution B, 4.54 g of 2-methylimidazole was dissolved in 1.5 mL of distilled water. Subsequently, solution A was slowly added to solution B and thoroughly mixed with a magnetic stirrer, during which the mixture acquired a milky appearance. After 30 minutes of stirring, the resultant suspension was separated by centrifugation for 20 minutes and washed twice with distilled water. Finally, the recovered material was dried at 80 °C for 24 hours to ensure complete evaporation of the residual solvent.

2.1.4. Preparation of Fe_3O_4@ZIF-8@Ag_2O. A nanocomposite was prepared by first adding 0.18 g of zinc nitrate hexahydrate ($Zn(NO_3)_2 \cdot 6H_2O$) and 0.5 g of iron oxide (Fe_3O_4) to 40 mL of a 2-methylimidazole solution. The mixture was sonicated for 45 minutes to achieve a uniform dispersion and prevent sedimentation.[39] Separately, 0.01 g of pre-synthesized Ag_2O nanoparticles was dispersed in 10 mL of distilled water by magnetic stirring, and the dispersion was further sonicated to ensure homogeneity. The Ag_2O dispersion was then combined

with 10 mL of the ZIF-8 solution and further sonicated. The resulting Fe_3O_4@ZIF-8@Ag_2O nanocomposite was isolated using a magnet and dried overnight at 110 °C. The synthesized nanocomposite can be reused for a long time due to the Fe_3O_4 nanoparticles. Some research indicates that magnetic Fe_3O_4 nanocomposites can be effectively separated and reused for multiple cycles in the removal of bacteria or other pollutants, with some decrease in efficiency over time due to factors like surface fouling. Studies have shown that the stability and reusability of Fe_3O_4 nanocomposites can be enhanced by immobilizing them on supporting materials like cellulose or by surface modifications that prevent the aggregation and leaching of active agents.[40–42]

2.2. Micro-organism culturing

Escherichia coli strain ATCC 25922 was obtained from the Microbiology Laboratory of the Education Development Center of Medical Sciences at Tabriz University. The strain was cultured on Plate Count Agar for 24 hours at 37 °C. Following incubation, the bacterial suspension was adjusted to a 0.5 McFarland standard (approximately 1.5×10^8 CFU mL^{-1}) and subsequently diluted to a concentration of 10^5 CFU mL^{-1}. Serial dilutions were then performed to achieve concentrations of 10^2, 10^3, and 10^4 CFU mL^{-1}.[43] In each dilution step, 1 mL from the previous dilution was transferred into 9 mL of deionized water, a process that was repeated until the desired concentration range for counting was obtained.

2.3. The column reactor setup for antibacterial application

The experiment was performed using a glass column packed with the antibacterial nanocomposite. Two layers of glass wool were positioned at the top of the column to prevent loss of the nanocomposites, while glass beads were incorporated to ensure the uniform flow of the inlet fluid. A peristaltic pump was employed to convey the fluid upward through the column, with the nanocomposite charged from the top. A schematic representation of the experimental setup is provided in Fig. 1.

A solenoid coil was uniformly wrapped around the column at equidistant intervals. Upon the application of a DC through the coil, a magnetic field was generated.

2.4. Magnetic column reactor

The column reactor was recognized as a critical component in the industrial-scale design of water treatment systems. This study aimed to evaluate the effects of various process parameters, including the stability and survival of *Escherichia coli* in aqueous solution and PBS, the performance of the Fe_3O_4@ZIF-8@Ag_2O nanocomposite, and the influence of an applied magnetic field. A column reactor, measuring 32 cm in length with an inner diameter of 2 cm, was employed. Prior to the experiment, the reactor and all associated instruments were pre-wetted with autoclaved distilled water (120 °C, 30 minutes). Subsequently, distilled water was passed through the reactor to remove any dry granules of the Fe_3O_4@ZIF-8@Ag_2O nanocomposite.

During the trial phase, the prepared contaminant water was pumped through the reactor at a flow rate of 10 mL per minute using a peristaltic pump. This flow rate was selected based on the reactor dimensions and the desired residence time of the bacteria within the reactor, thereby optimizing the contact between the bacteria and the nanoparticles to improve the bacterial removal efficiency. While the solution flowed downward through the reactor, a magnetic field was applied using a solenoid coil powered by a 12 V DC power supply at a current of 0.2 A. The treated water, referred to as the effluent, was collected from the top outlet of the reactor at specific time intervals (10, 20, 30, 40, 50, and 60 minutes) for sampling.

To determine the kinetic reaction parameters, the experimental results were fitted to the Chick–Watson and Weibull models. The Chick–Watson kinetic model is represented by the following equation:

$$\log(C_e) = \log(C_i) - k_{max}t \quad (1)$$

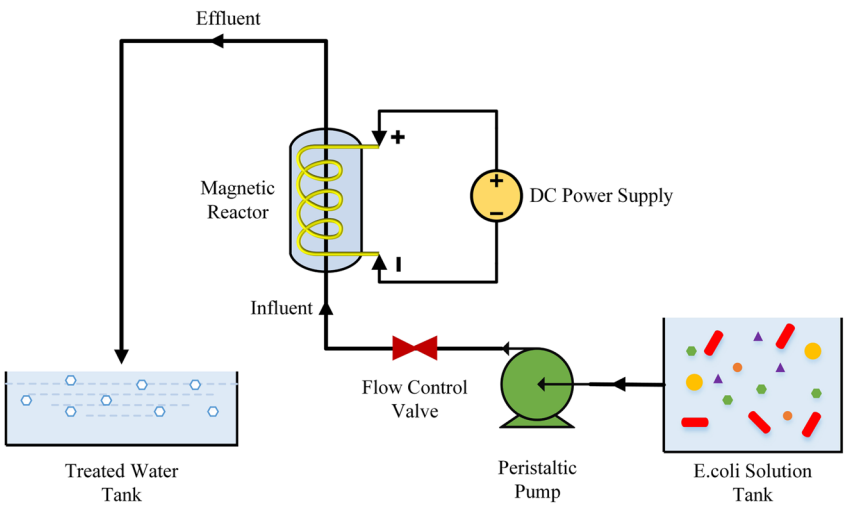

Fig. 1 Schematic of the experimental setup.

where C_i and C_e are the influent and effluent *E. coli* concentrations (CFU mL^{-1}), respectively. k_{max} is the rate constant of the reaction (mol L^{-1} min^{-1}) and t is the contact time of the reaction (s). The Weibull model equation is expressed as the following relation:[44]

$$\log(C_e) = -\left(\frac{t}{\delta}\right)^{\beta} + \log(C_i) \quad (2)$$

where δ is the time for the first decimal reduction (min^{-1}) and β is the shape parameter (concave curves, $\beta < 1$; convex curves, $\beta > 1$), respectively. The models and kinetic parameters were obtained using the Solver tool and the GInaFiT Add-in version 1.7 (Geeraerd and Van Impe Inactivation Model Fitting Tool).[45]

The RMSE equation was given by Mecha *et al.*, 2020, as follows:[46]

$$\mathrm{RMSE} = \sqrt{\frac{\sum_{i=1}^{N}\left(y_{\mathrm{exp},i} - y_{\mathrm{pre},i}\right)^2}{N}} \quad (3)$$

where N is the number of observations, $y_{exp,i}$ is the experimental observation value, and $y_{pre,i}$ is the model prediction value. The percentage removal of *E. coli* was calculated using the following equation:[47]

$$R\% = \frac{C_i - C_e}{C_i} \times 100 \quad (4)$$

where C_i is the *E. coli* concentration in the influent (CFU mL^{-1}), and C_e is the *E. coli* concentration in the effluent (CFU mL^{-1}).

Solenoid wire coils were employed to generate a controlled magnetic field, a configuration that has found numerous applications in industry. In this study, the magnetic field generated by the coils surrounding the MNPs within the reactor was utilized to enhance particle stability in the bed, increase Brownian motion and particle collisions, and ultimately improve the bacterial removal efficiency. The system's effectiveness was further optimized by adjusting its parameters. The magnetic field was oriented to induce a counter-current flow of the Fe_3O_4@ZIF-8@Ag_2O nanocomposite relative to the influent contaminant water. An increase in the magnetic field correspondingly reduced the velocity profile of the particles, which extended the contact time between the *E. coli* bacteria and the adsorbents, resulting in a higher percentage of *E. coli* removal in the effluent. Conversely, the Brownian motion of the particles within the reactor led to an increasing temperature profile and a decreasing concentration profile. Although the decreased concentration extended the reaction time, the elevated temperature posed challenges by potentially disrupting data measurement processes. Consequently, temperature control was deemed crucial, and the temperature profile was regulated through the careful selection of the solenoid wire coil's design parameters, such as the wire material, length, cross-sectional area, and the applied voltage and current. Efforts were made to maintain a constant temperature profile throughout the experiment to isolate the effects of the magnetic field and MNPs on *E. coli* removal from the aqueous solution. Therefore, the calculations for the design of the solenoid wire coil were performed as follows.

The electric power of a wire (W) is given by Joule's law:

$$P = RI^2 \quad (5)$$

where R is the resistance of the wire (Ω) and I is the electric current (A).

The energy balance was used to obtain temperature distribution equations in cylindrical coordinates.

The energy balance is obtained from the following equation:

$$Q_{in} - Q_{out} + Q_{gen} - Q_{con} = Q_{cum} \quad (6)$$

where Q_{in}, Q_{out}, Q_{gen}, Q_{con}, and Q_{cum} are the energy input, energy output, generated energy, energy consumption, and energy cumulative, respectively.

The rate of heat generated (W m^{-3}) obtained from energy balance is calculated as follows:[48]

$$\dot{q} = \frac{R \times I^2}{\pi \times r^2 \times L} \quad (7)$$

where r is the radius of the wire (m) and L is the length of the wire (m).

Also, to obtain the local temperature at each location of the wire, the differential equation was calculated as follows:[49]

$$\frac{1}{r}\frac{\mathrm{d}}{\mathrm{d}r}\left(r\frac{\mathrm{d}T}{\mathrm{d}r}\right) = -\frac{\dot{q}}{k} \quad (8)$$

where T is the temperature (K) and k is the thermal conductivity (W m^{-1} K^{-1}). Then, the temperature distribution is given by integrating eqn (8):

$$T = -\frac{\dot{q} \times r^2}{4k} + C_1 \ln r + C_2 \quad (9)$$

By considering the following boundary conditions,

$$r = 0\text{: } T = \text{infinite: } C_1 = 0 \quad (10)$$

and

$$r = R: \quad T = T_s: \quad C_2 = T_s + \frac{\dot{q} \times R^2}{4k} \quad (11)$$

The final solution for the temperature distribution is then

$$T - T_s = \frac{\dot{q} \times R^2}{4k}\left(R^2 - r^2\right) \quad (12)$$

To obtain T_0, eqn (11) is transformed to give:

$$T_0 - T_s = \frac{\dot{q} \times R^2}{4k} \quad (13)$$

where T_0 is the temperature at $r = 0$ and T_s is the surface temperature.

The Biot number is given by the following:[49]

$$B_i = \frac{h \times L_c}{k} \quad (14)$$

where h is the convection heat transfer coefficient (W m^{-2} K^{-1}), L_c is the characteristic length (m), and k is the thermal conductivity (W m^{-1} K^{-1}).

The lumped capacitance method is defined by the following equation:[49]

$$\frac{T - T_a}{T_i - T_a} = e^{-\frac{t}{\tau}} \quad (15)$$

where T is the final temperature (K), T_a is the temperature of the environment (K), T_i is the initial temperature of the wire (K), t is the time (s), and τ is the time constant (s).

The temperature difference between the center and the surface of the wire was calculated. Maintaining a constant temperature profile during the experiment was a key objective of this study, necessitating careful selection of the design parameters for the solenoid wire coil. Assuming the surface temperature of the wire is room temperature (25 °C), the temperature at the center of the wire, as given by eqn (13), is 26 °C. This indicates that there is too little difference between the center and surface temperatures of the wire for the generated heat to affect the inactivation of *E. coli*. In addition, using eqn (14), the Biot number was obtained as 3.1×10^{-6}, which can be considered lumped (<0.1). Then, by using eqn (15), the final surface temperature of the wire was obtained as 25 °C, leading to the conclusion that there is no significant difference between the initial and final temperatures (constant temperature) over a period of 60 minutes.

Table 1 Specifications of the designed solenoid wire coil

Description	Specifications
Wire material	Copper
Wire diameter, D	0.2 mm
Wire length, L	106 m
Number of turns, N	1680
Resistivity of wire coil, ρ	1.72×10^{-8} Ω m
Resistance of wire coil, R	58 Ω
Thermal conductivity, k	400 W m^{-1} K^{-1}
Convection heat transfer coefficient, h	25 W m^{-2} K^{-1}
DC power supply, V	12 V
Current flow, I	0.2 A

The specific specifications of the designed coil are outlined in Table 1 in the supplemental material, and a schematic of the coil is provided in Fig. 2.

The generated magnetic field (mT) of the solenoid wire coil is given by Hart:[50]

$$B = \mu_0 \frac{N \times I}{L} \quad (16)$$

where μ_0 is the vacuum permeability ($4\pi \times 10^{-7}$ N A^{-2}), N is the number of turns of the wire, I is the electric current (A), and L is the length of the wire (m). According to the data in Table 1, the strength of the magnetic field is obtained from eqn (16).

The hydrodynamic parameters existing in the reactor, including flow velocity, Reynolds number, diffusivity, and mass transfer coefficient, along with the utilized formulas, based on the calculations derived, are summarized in Table 2. The hydrodynamic regime of the magnetic column reactor, designed for *E. coli* removal, is characterized by a laminar flow profile, as evidenced by a Re = 10.63, while the utilized physical values are listed in Table 2. The superficial velocity is derived from a volumetric flow rate of 10 mL min^{-1} and the column cross-sectional area. Assuming a bed porosity of 0.4, the interstitial velocity is 0.001329 m s^{-1}. This low Re < 2000 confirms laminar flow, which promotes stable and uniform fluid movement, facilitating efficient contact between the Fe_3O_4@ZIF-8@Ag_2O magnetic nanocomposites and *E. coli* cells. The diffusion-limited regime is further indicated by a low mass transfer, estimated using the Wilson–Geankoplis correlation, with a particle Reynolds number of 1.329, Schmidt number 5×10^5, and Sherwood number of 95.20. The molecular diffusivity of *E. coli* in water underscores the slow mass transfer, which is overcome by the 2 mT magnetic field. The laminar flow and diffusion-limited conditions, combined with magnetic effects, ensure optimized nanoparticle–bacteria interactions for effective water treatment.

2.5. Characterization

Field emission scanning electron microscopy (FESEM) images were acquired using a TESCAN MIRA3-FEG scanning electron microscope equipped with an energy-dispersive X-ray (EDX)

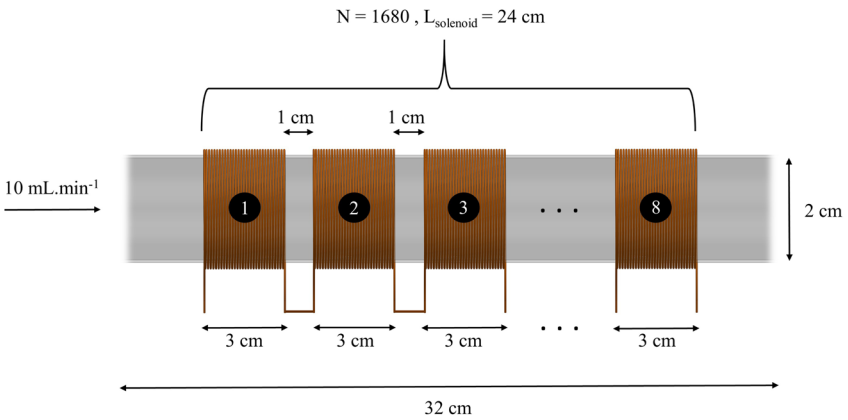

Fig. 2 Schematic of the designed solenoid wire coil.

Table 2 Hydrodynamic parameters of the reactor flow

Parameter	Value	Formula	Description/notes
Superficial flow velocity (u)	0.0005317 m s^{-1} (0.5317 mm s^{-1})	$u = Q/A$	$Q = 1.67 \times 10^{-7}$ m^3 s^{-1}, $A = \pi(0.01)^2 = 3.1416 \times 10^{-4}$ m^2
Interstitial flow velocity (u_i)	0.001329 m s^{-1}	$u_i = u/\varepsilon$	Assumed porosity = 0.4. Adjusts the superficial velocity for packed bed
Reynolds number (Re)	10.63	$Re = \rho u d/\mu$	$\rho = 1000$ kg m^{-3}, $u = 5.317 \times 10^{-4}$ m s^{-1} $d = 0.02$ m $\mu = 1.0 \times 10^{-3}$ Pa s Confirms laminar flow (Re < 2000)
Diffusivity (D)	2×10^{-9} m^2 s^{-1}	—	Provided in the text for *E. coli* in water, consistent with the literature for bacterial diffusion
Mass transfer coefficient (k_L)	1.904×10^{-7} m s^{-1}	$Sh = k_L d_p/D = 1.09(Re_p \cdot Sc)^{1/3}$	Wilson–Geankoplis correlation used. $d_p = 0.00$ m (assumed for glass beads) $Re_p = 1.329$ $Sc = 5 \times 10^5$ $Sh = 95.20$ Indicates a diffusion-limited regime
Particle Reynolds number (Re_p)	1.329	$Re_p = \rho u_i d_p/\mu$	$u_i = 1.329 \times 10^{-3}$ m s^{-1} $d_p = 0.00$ m Used for mass transfer calculation
Schmidt number (Sc)	5×10^5	$Sc = \mu/\rho D$	$\mu = 1.0 \times 10^{-3}$ Pa s $\rho = 1000$ kg m^{-3} $D = 2 \times 10^{-9}$ m^2 s^{-1} High Sc indicates diffusion-dominated transport
Sherwood number (Sh)	95.20	$Sh = 1.09(Re_p \cdot Sc)^{1/3}$	Derived from the Wilson–Geankoplis correlation for laminar flow in packed beds

detector, which enabled the examination of nanoparticle morphology and surface characteristics. X-ray diffraction (XRD) analysis was performed using a Tongda TD-3700 instrument to ascertain the composition of the nanoparticles and to identify the functional groups present on their surfaces. The magnetic properties were evaluated at room temperature using a vibrating sample magnetometer (VSM) integrated with a FORC-MDKF system.

3. Results and discussion

3.1. Nanocomposite characterization

The structures of Fe_3O_4, Ag_2O, ZIF-8, and the Fe_3O_4@ZIF-8@Ag_2O nanocomposite were characterized using XRD measurements, as shown in Fig. 3. The characteristic diffraction peaks of the synthesized Fe_3O_4 nanoparticles are in complete agreement with the standard Fe_3O_4 pattern (JCPDS 19-0629),[51] confirming the successful synthesis of Fe_3O_4. The diffraction peaks of Fe_3O_4 at 2θ angles of 30.26° (220), 35.66° (311), 43.31° (400), and 57.12° (511) indicate that the Fe_3O_4 structure remained intact during the synthesis of the Fe_3O_4@ZIF-8@Ag_2O nanocomposite. The Ag_2O sample exhibited characteristic diffraction peaks at 26.82° (110), 32.64° (111), 37.96° (200), and 54.39° (220), consistent with the face-centered cubic (FCC) crystalline phase of silver(I) oxide (JCPDS 75-1532).[52] Additionally, the diffraction peaks of ZIF-8 at 10.55° (002), 12.34° (112), 14.63° (022), 18.05° (222), and 22.52° (114) were in agreement with the standard ZIF-8 pattern (JCPDS 76-1509),[53] further confirming the crystalline nature of the ZIF-8 sample.

Bragg's law[54] and Scherrer's equation[55] were used to determine the mean size of the particles, as follows:

$$n\lambda = 2d \quad \sin \quad \theta \tag{17}$$

$$X = \frac{k \times \lambda}{\mathrm{FWHM} \times \cos\theta} \tag{18}$$

where n is a positive integer (1.0), λ is the X-ray wavelength radiation (nm), d is the distance between the lattice planes, X is the mean crystallite size (nm), k is the shape factor (0.9), FWHM is the full width at half maximum of the peaks (radians), and θ is the glancing angle (radians). The mean crystallite sizes of Fe_3O_4, ZIF-8, and Ag_2O nanoparticles and the Fe_3O_4@ZIF-8@Ag_2O nanocomposite are 33 nm, 20.54 nm, 26 nm, and 30.62 nm, respectively.

The morphologies of Fe_3O_4, Ag_2O, ZIF-8, and the Fe_3O_4@ZIF-8@Ag_2O nanocomposite were examined using SEM, as shown in Fig. 4a, where the Fe_3O_4 particles exhibit a clustered shape with rough angles. These particles serve as the core of the nanocomposite. Fig. 4b illustrates the spherical shape of the Ag_2O particles. Fig. 4c displays the morphology of the ZIF-8 particles, which have a multifaceted shape with slightly rounded corners that are arranged in a regular pattern. In this study, the ZIF-8 particles act as the shell of the nanocomposite. The uniform distribution of ZIF-8 on the surface of the Fe_3O_4 core particles, as demonstrated in Fig. 4d, indicates that the ZIF-8 shell completely covers the core. The surface of the Fe_3O_4@ZIF-8@Ag_2O nanocomposite in Fig. 4d appears rougher than the surface of the unmodified Fe_3O_4 nanoparticles in Fig. 4a, suggesting that the Fe_3O_4 particles have been successfully loaded with ZIF-8 and Ag_2O nanoparticles. Elemental

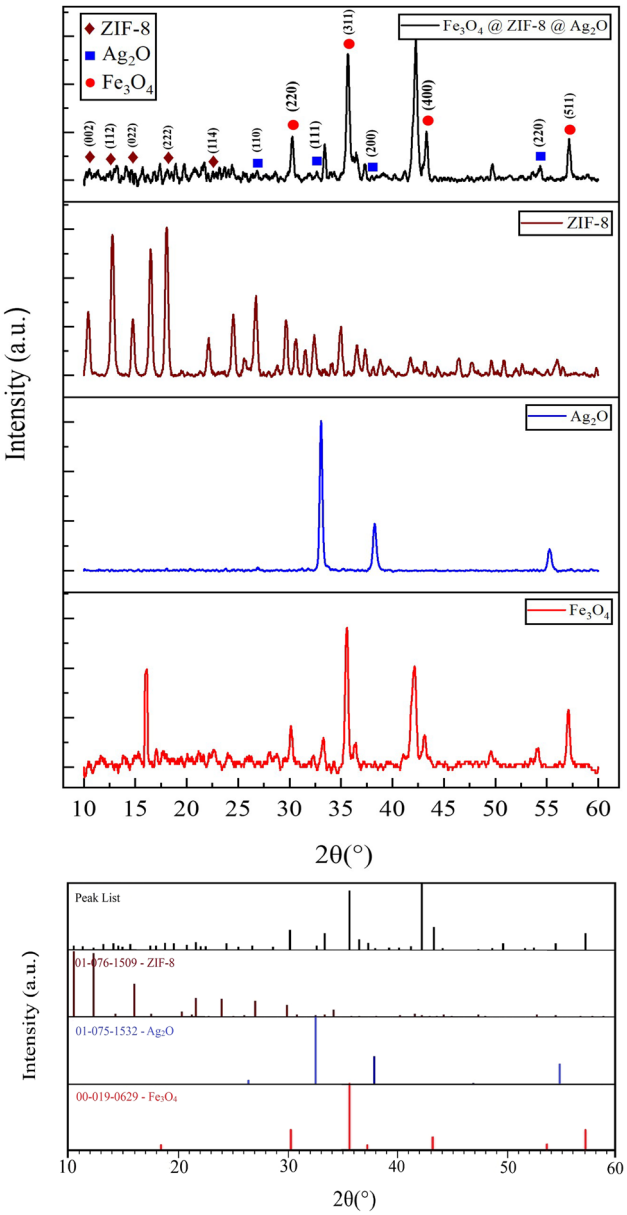

Fig. 3 XRD patterns of Fe_3O_4, Ag_2O, and ZIF-8 nanoparticles, and the Fe_3O_4@ZIF-8@Ag_2O nanocomposite.

mapping analyses were conducted to further confirm the distribution of ZIF-8 and Ag_2O on the Fe_3O_4 nanoparticles. The images in Fig. 4g and l illustrate the distribution of these elements throughout the sample. The image in Fig. 4f shows a uniform distribution of the elements on the Fe_3O_4@ZIF-8@Ag_2O nanocomposite Fig. 4e, indicating the successful formation of a well-defined shell structure.

The EDX spectra show the organic content in the structure of the composite. The composition of the Fe_3O_4@ZIF-8@Ag_2O sample includes zinc (Zn), iron (Fe), silver (Ag), oxygen (O), nitrogen (N), and carbon (C). The EDX spectrum of Fe_3O_4@ZIF-8@Ag_2O MNCs is presented in Fig. 4m. The atomic percentages of Zn, Fe, Ag, O, N, and C in the Fe_3O_4@ZIF-8@Ag_2O nanocomposite, as determined by EDX analysis, were found to

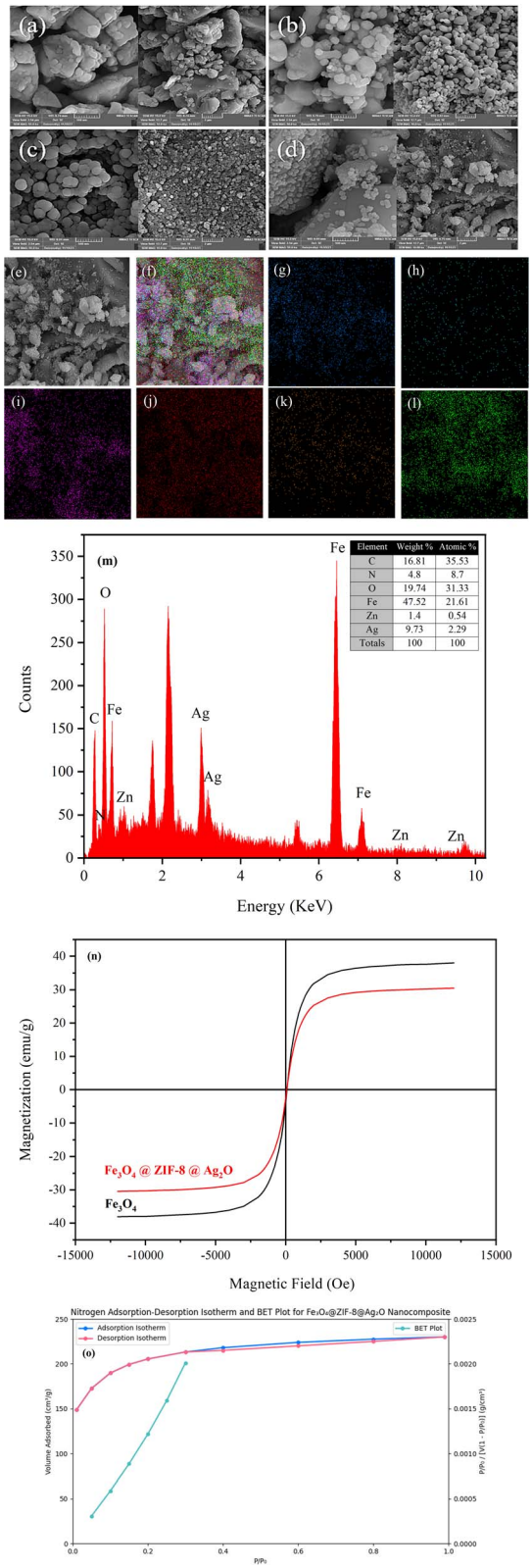

Fig. 4 SEM images of Fe_3O_4 (a), Ag_2O (b), ZIF-8 (c), and Fe_3O_4@ZIF-8@Ag_2O (d). Elemental maps of the Fe_3O_4@ZIF-8@Ag_2O nanocomposite (e). Images of the elemental distribution in the nanocomposite sample (f), C (g), Zn (h), Ag (i), Fe (j), N (k), and O (l). EDX spectrum of Fe_3O_4@ZIF-8@Ag_2O MNCs (m). VSM magnetization curves of Fe_3O_4 and Fe_3O_4@ZIF-8@Ag_2O (n). BET plot and adsorption–desorption plot for Fe_3O_4@ZIF-8@Ag_2O (o).

be in close agreement with the expected stoichiometry for the intended core–shell structure. Specifically, the observed Fe : Zn : Ag ratio approximates the theoretical molar balance for Fe_3O_4 (core), ZIF-8 (shell), and Ag_2O nanoparticles deposited on the surface. Minor deviations from stoichiometry are likely due to surface enrichment effects and partial coverage. The detectable presence of C and N further confirms the integration of the ZIF-8 framework, while the relative abundance of Ag validates the successful decoration with Ag_2O. Overall, the atomic ratios support the proposed architecture of Fe_3O_4@ZIF-8@Ag_2O.

Fig. 4n presents the magnetization curves of the prepared Fe_3O_4 nanoparticles and Fe_3O_4@ZIF-8@Ag_2O nanocomposite. The magnetic properties of these materials were investigated using a VSM at room temperature. The saturation magnetization values for the prepared Fe_3O_4 nanoparticles and Fe_3O_4@ZIF-8@Ag_2O nanocomposite were determined to be 38.10 emu g^{-1} and 30.47 emu g^{-1}, respectively. The decrease in saturation magnetization for the nanocomposite can be attributed to the non-magnetic properties of the ZIF-8 and Ag_2O nanoparticles coated on the Fe_3O_4 nanoparticles. This reduction in magnetization is advantageous, as it allows for the easy recovery of the MNCs from the reaction medium using an external magnetic field within a short time frame.

The Brunauer–Emmett–Teller (BET) analysis for the Fe_3O_4@ZIF-8@Ag_2O nanocomposite, as nitrogen adsorption–desorption data, provides insight into the material's surface area and porosity, which are critical for its application in bacterial removal from water. The BET plot, derived from adsorption data in the relative pressure range P/P_0 of 0.05–0.3, exhibits a linear relationship when plotting $P/P_0/V(1 - P/P_0)$ against P/P_0, indicating that the BET model is applicable for this material. The linearity of the plot suggests consistent adsorption behavior typical of microporous materials. From this plot, a linear regression yields an approximate slope of 0.0058 and an intercept of 0.0001, allowing the calculation of the monolayer adsorbed gas volume V_m as approximately 169.5 cm^3 g^{-1}. Using the BET equation, this corresponds to a specific surface area S_{BET} of approximately 735 m^2 g^{-1}, calculated with the nitrogen molecular cross-sectional area 0.162 nm^2 and molar volume at STP (22 414 cm^3 mol^{-1}). This surface area is lower than that of pure ZIF-8 (~1500–2000 m^2 g^{-1}) but higher than typical values for Fe_3O_4 (~20–50 m^2 g^{-1}) or Ag_2O (~10–30 m^2 g^{-1}), reflecting the composite's structure where the microporous ZIF-8 shell dominates but is moderated by the non-porous Fe_3O_4 core and Ag_2O nanoparticles.

The nitrogen adsorption–desorption isotherm further characterizes the nanocomposite's porosity. The adsorption data show a steep increase in the volume adsorbed at low relative pressures $P/P_0 < 0.1$, reaching 148.6 cm^3 g^{-1} at $P/P_0 = 0.01$, and 172.5 cm^3 g^{-1} at $P/P_0 = 0.05$, indicative of strong micropore filling typical of ZIF-8. The isotherm plateaus at higher pressures, with volumes of 213.2 cm^3 g^{-1} at $P/P_0 = 0.3$ and 230.0 cm^3 g^{-1} at $P/P_0 = 0.99$, suggesting limited additional adsorption beyond micropore capacity. The desorption branch closely follows the adsorption curve, with volumes of 225.0 cm^3 g^{-1} at $P/P_0 = 0.8$ and 220.0 cm^3 g^{-1} at $P/P_0 = 0.6$, exhibiting minimal hysteresis in the $P/P_0 = 0.4$–0.9 range. This behavior classifies the isotherm as Type I(b) according to IUPAC standards, characteristic of microporous materials with pore sizes close to the nitrogen molecule's diameter. The minimal hysteresis suggests a predominantly microporous structure, with slight mesoporosity possibly introduced by the integration of Fe_3O_4 and Ag_2O, which aligns with the composite's design as a ZIF-8 shell encasing a Fe_3O_4 core with Ag_2O nanoparticles on the surface.

These BET results are significant for the nanocomposite's application in *E. coli* removal, as described in the manuscript. The high surface area of 735 m^2 g^{-1} enhances the material's ability to interact with bacterial cells, facilitating mechanisms such as ion release (Ag^+ and Zn^{2+}), reactive oxygen species generation, and physical penetration of cell walls, as noted in the manuscript's mechanistic insights. The microporous nature, confirmed by the Type I(b) isotherm, supports efficient adsorption and interaction at the nanoscale, which is critical for the observed 99.83% *E. coli* removal efficiency under magnetic field conditions. The predicted surface area and isotherm type are consistent with literature values for similar ZIF-8-based composites, where the incorporation of non-porous components like Fe_3O_4 and Ag_2O reduces the surface area compared to pure ZIF-8, but maintains sufficient porosity for effective antibacterial performance. These findings underscore the suitability of the Fe_3O_4@ZIF-8@Ag_2O nanocomposite for water treatment applications, leveraging its high surface area and microporous structure to achieve rapid and efficient bacterial inactivation.

3.2. *E. coli* culturing for the regulation of the experiment

Maintaining a stable initial concentration of *E. coli* bacteria for an hour in the contaminated water tank was a significant challenge in this research. To address this, we used distilled water and PBS as host solvents to sustain *E. coli* viability and concentration. PBS was prepared by dissolving a 1 g tablet in 200 mL of distilled water. Cultured *E. coli* were then added separately to 200 mL of water and PBS. Samples were collected at 10-minute intervals for one hour. Fig. 5 illustrates the survival of *E. coli* in both distilled water and 0.5 wt% PBS. As shown, the concentrations of *E. coli* in aqueous solution and 0.5 wt% PBS are 6.25, 5.97, 5.46, 5.15, and 6.31, 6.47, 6.42, and 6.27 log CFU mL^{-1}, respectively. Fig. 5a–d show the *E. coli* colonies observed on agar plates from two experimental replicates. The data in Fig. 5e demonstrate the average concentrations of *E. coli* in distilled water and 0.5 wt% PBS, determined from two experimental replicates. The error bars represent the standard deviation. As shown, the concentration of *E. coli* in distilled water decreased over time, while the concentration in PBS remained relatively constant. This stability in PBS offers an advantage for preparing initial *E. coli* concentrations in contaminated water, as it helps to prevent spontaneous bacterial death during experimentation. Given the small error bars in Fig. 5e ($n = 3$ independent measurements), it can be concluded that the variability in *E. coli* concentration measurements at a given time point is minimal.

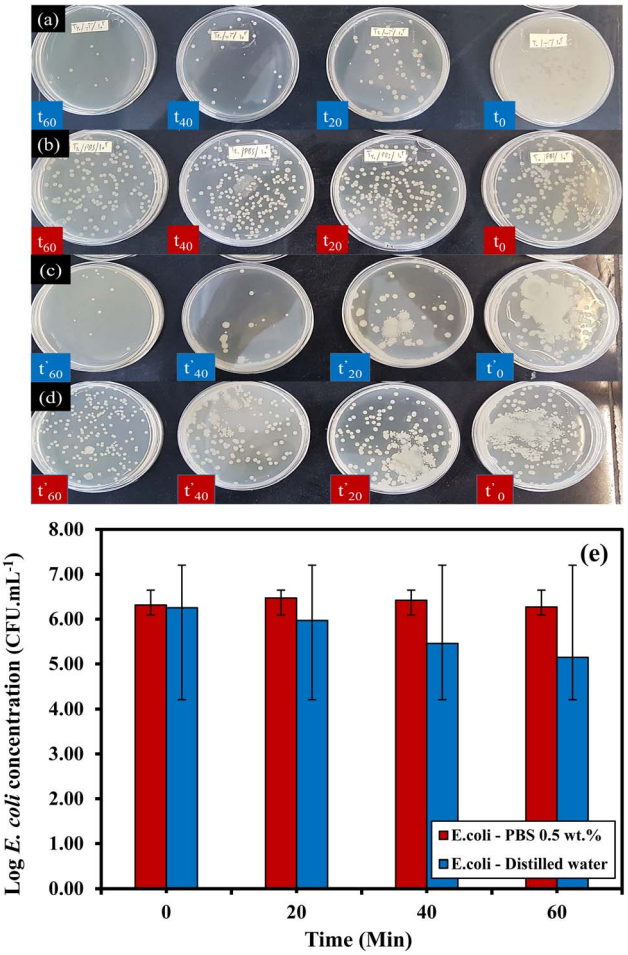

Fig. 5 *E. coli* colonies incubated on agar plates for different times from t_0 to t_{60}: (a) *E. coli* colonies-water; (b) *E. coli* colonies-PBS, and for the second iteration from t_0' to t_{60}'; (c) *E. coli* colonies-water; (d) *E. coli* colonies-PBS, and surviving *E. coli* in PBS and distilled water *versus* different contact times. (e) Error bars indicate the standard deviation (n = 3 independent measurements).

3.3. The effect of a magnetic field on the removal of *E. coli*

The results of the survival experiments indicated that *E. coli* bacteria can survive longer in PBS than in water. Consequently, *E. coli*-PBS mixtures were used to investigate the impact of a magnetic field on *E. coli* removal from water. Two experimental setups were employed: one without a magnetic field and one with a 2 mT magnetic field applied to MNPs in the reactor. Fig. 6a depicts the stability of MNPs within the reactor post-experiment. The particles, initially confined by the magnetic field, either adhered to the reactor walls or were released into the solution.

For both experimental setups, an initial *E. coli* concentration of 3.57×10^5 CFU mL^{-1} was maintained in the *E. coli*-PBS-water mixture. Effluent samples were collected at 10-minute intervals. As illustrated in Fig. 6b, the concentrations of *E. coli* in the presence of 0.05 wt% composite were recorded as 5.55, 5.04, 4.62, 4.43, 4.37, 4.14, and 3.95 log CFU mL^{-1}, respectively. The data indicate that the presence of MNPs significantly reduces the *E. coli* concentration in comparison to the control experiment (Fig. 5). The removal mechanism involves the interaction

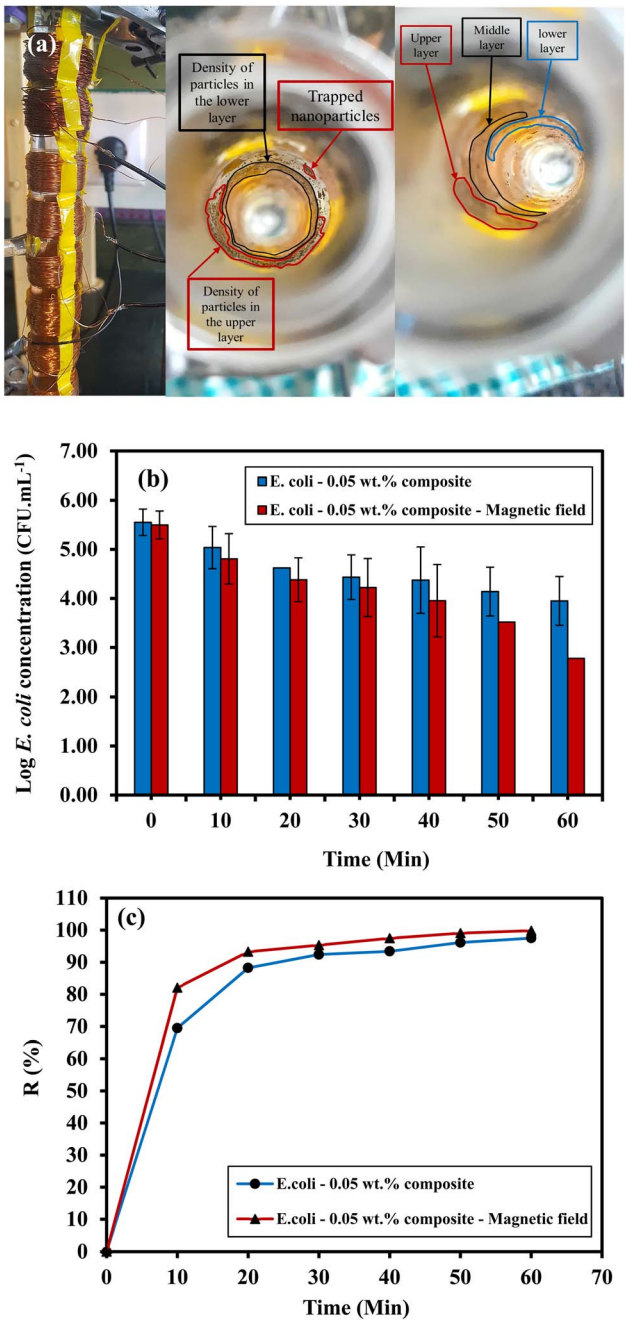

Fig. 6 Images of the magnetic reactor and trapped magnetic particles in the column (a). Effect of a magnetic field on the removal of *E. coli* concentrations *versus* different contact times; error bars indicate the standard deviation (b). Removal percentage of *E. coli* concentrations *versus* different contact times (c).

between *E. coli* bacteria and MNPs within the reactor. The magnetic field generated around the reactor was induced by the copper solenoid coil, stabilizing the MNPs inside the reactor.

The bacterial cell, composed of proteins, deoxyribonucleic acid (DNA), and enzymes, is susceptible to disruption by the ions released from Fe_3O_4@ZIF-8@Ag_2O nanocomposites. These ions interfere with adenosine triphosphate (ATP) production and DNA replication. Furthermore, the antibacterial activity of silver-based nanomaterials can be attributed to multiple

mechanisms, including the disruption of cell membrane permeability after attachment to the bacterial wall, inactivation of proteins through binding with sulfhydryl groups, interference with the respiratory chain leading to oxidative stress, and stimulating the Ag_2O and Fe_3O_4 nanoparticles by a magnetic field that causes electrons to be captured at the active sites. Afterward, the electrons interact with oxygen (O_2) to produce ROS, thereby enhancing the antimicrobial effectiveness of Ag_2O NPs, and inhibition of DNA replication, ultimately causing lipid damage.[56] MNPs, possessing a larger surface area than bacterial cells, can penetrate the bacterial cell walls upon collision. This penetration disrupts key enzymatic functions essential for the bacterial cell cycle, leading to bacterial inactivation and cell death.[21,57] In contrast, previous studies have demonstrated that nanoparticles with surface areas comparable to bacterial cells are incapable of penetrating the cell membrane. Consequently, nanoparticles with larger surface areas exhibit greater efficacy in compromising the bacterial cell wall.[58] Under the influence of a magnetic field, the concentrations of *E. coli* in the presence of 0.05 wt% composite were recorded as 5.50, 4.81, 4.38, 4.22, 3.95, 3.52, and 2.78 log CFU mL^{-1}, respectively. Over a 60-minute period, the *E. coli* concentration decreased by 29.6% in the presence of a magnetic field due to collisions between *E. coli* and nanoparticles with each other in opposite directions in the column, which was a more pronounced reduction than under conditions without a magnetic field. Fig. 6b demonstrates a significant decrease in *E. coli* concentration under the influence of a magnetic field compared to conditions without it. This suggests that the application of a magnetic field enhances the removal efficiency of *E. coli* bacteria. The stabilization of MNPs within the reactor by the magnetic field confines them to the central region around the wire coils, increasing the contact time between the nanoparticles and bacterial cells, thereby optimizing *E. coli* removal from the aqueous solution. Notably, the standard deviation of *E. coli* concentration data at 40-minutes under magnetic field conditions reached a maximum of 75%.

Fig. 6c illustrates the percentage of *E. coli* removal at various contact times. Under magnetic field conditions, *E. coli* removal rates reached 82.07% and 99.83% at 10 and 60-minutes, respectively. In contrast, in the absence of a magnetic field, the removal rates were comparatively lower, reaching 69% and 98% at 10 and 60-minutes, respectively. Consequently, this result demonstrates a significant increase in the *E. coli* removal rate compared to the 74.2% observed by Chaudhary *et al.*[59] when Ag-based nanoparticles were used but without a magnetic field.

3.4. Kinetic modelling of the *E. coli* removal

The experimental data were validated by fitting the Chick–Watson and Weibull models, as illustrated in Fig. 7 and 8. Fig. 7 displays the predicted *E. coli* effluent concentrations for both models under conditions with and without a magnetic field over various contact times. The close correspondence between the predictions and observed data, supported by high coefficients of determination ($R^2 > 0.9$), confirms the robustness of both models. Notably, the Chick–Watson model achieved R^2 values of 0.9261 without and 0.9623 with the magnetic field, while the Weibull model

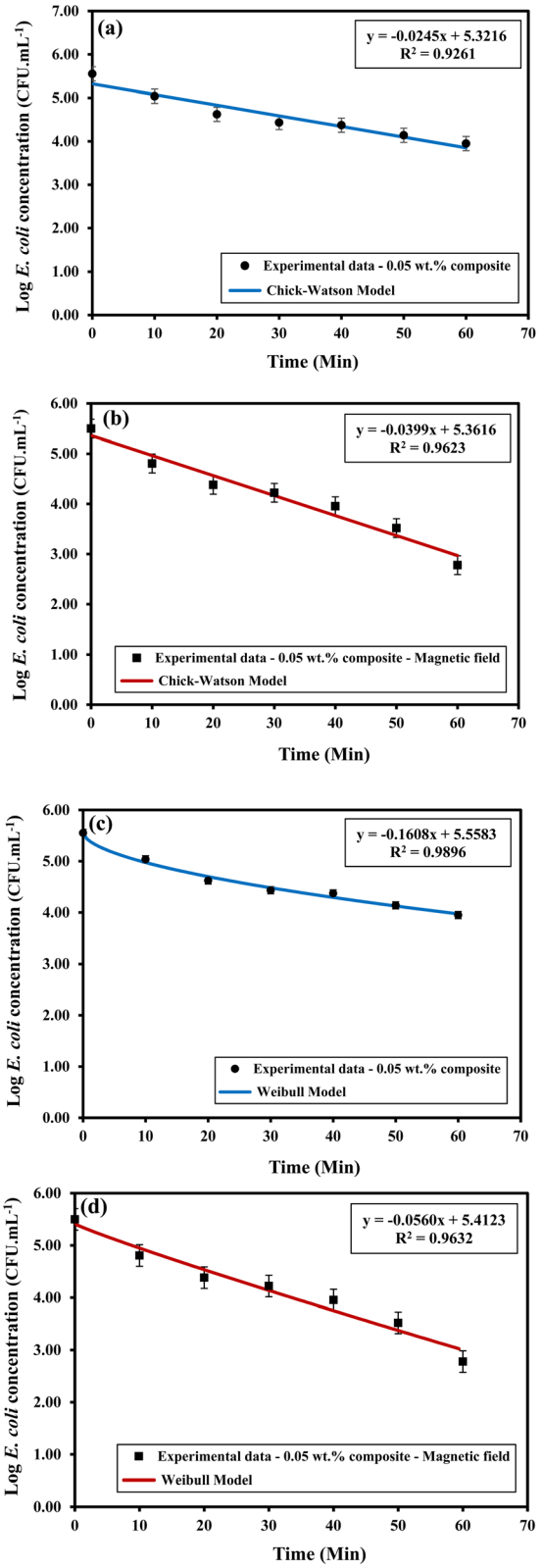

Fig. 7 Fitted models with experimental data: (a) the Chick–Watson model without the magnetic field, (b) the Chick–Watson model with the magnetic field, (c) the Weibull model without the magnetic field, and (d) the Weibull model with the magnetic field. Error bars represent the average deviation between the observed and predicted values.

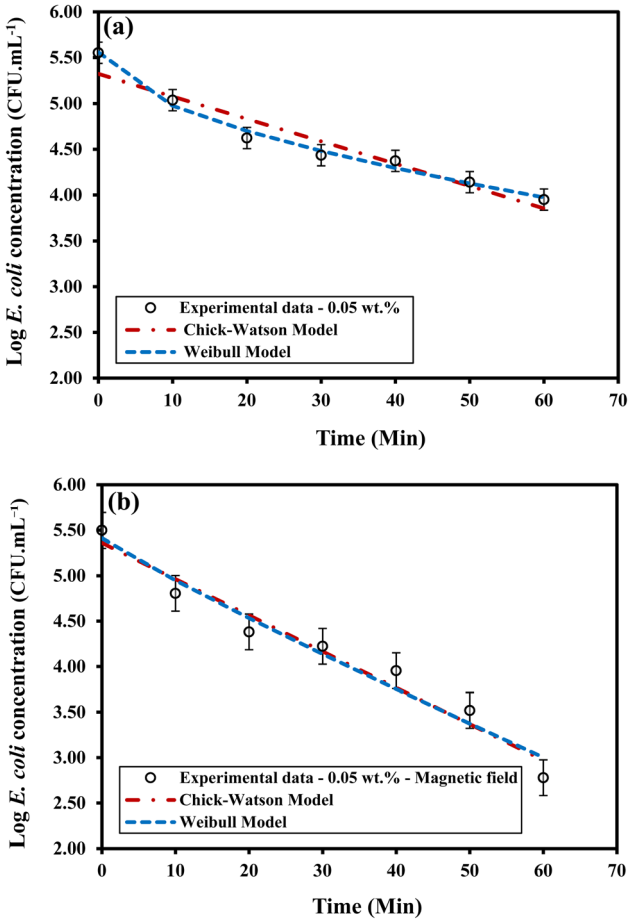

Fig. 8 Fitted model variations with experimental data: (a) without a magnetic field and (b) with a magnetic field. Error bars indicate the average deviation between the observed and predicted values.

recorded R^2 values of 0.9896 and 0.9632, respectively. Although the Chick–Watson model (Fig. 7b) reveals a more pronounced effect of the magnetic field on inactivation, the Weibull model indicates the highest accuracy in the absence of the field. The error bars in Fig. 7 represent the mean deviation between observed and predicted values, further attesting to the precision of the model fits. Alikhani *et al.*[60] reported their R^2 values and rate constants (k) for the removal of *E. coli* from aqueous solutions using a photocatalytic method. Their R^2 values were 0.935, 0.943, and 0.952, and the corresponding rate constants (k) were 0.024, 0.0143, and 0.0119 (min^{-1}) at initial concentrations of 1.5×10^4, 1.5×10^6, and 1.5×10^8 (CFU mL^{-1}), respectively. In contrast, the present study yielded R^2 and k values of 0.9623 and 0.092 (min^{-1}), respectively, at initial concentrations of 1.5×10^5 (CFU mL^{-1}), which are larger than those reported in the cited paper. These results show that upon inactivation, the magnetic field can further affect *E. coli* from water in comparison with the photocatalytic method without a magnetic field.

Fig. 8 further compares the variations of the fitted models under both experimental conditions, where superior accuracy is observed under the magnetic field influence.

The kinetic parameters derived from the regression analyses are summarized in Table 3. Without a magnetic field, the Chick–Watson model produced a k_{max} of 0.056 and an initial *E. coli* concentration ($\log_{10}(C_i)$) of 5.32, with an R^2 of 0.926 and an RMSE of 0.16. Under the same conditions, the Weibull model yielded a shape parameter (β) of 0.56, a scale parameter (δ) of 26.31, an initial $\log_{10}(C_i)$ of 5.56, an R^2 of 0.989, and an RMSE of 0.07. The low R^2 value for the Chick–Watson model could be due to the absence of a magnetic field, which indicates a poor fit. When a magnetic field was applied, the Chick–Watson model's k_{max} increased to 0.092 and the initial $\log_{10}(C)$ slightly to 5.36, with an improved R^2 of 0.962 (RMSE = 0.18), indicating an enhanced inactivation rate. Concurrently, the Weibull model exhibited an increase in β to 0.92 and a decrease in δ to 23.04, while the initial concentration remained unchanged, though its R^2 dropped to 0.963 with an RMSE of 0.21.

These results collectively suggest that the magnetic field enhances *E. coli* inactivation by increasing the kinetic rate constant in the Chick–Watson model and modifying the Weibull parameters, leading to a more pronounced initial inactivation phase. Despite a minor reduction in the Weibull model's performance under magnetic conditions, both models effectively characterize the bacterial removal process, with the Chick–Watson model showing a superior fit when the magnetic field is present.

3.5. Mechanistic insights into magnetic field-enhanced *E. coli* removal

The application of a 2 mT magnetic field significantly enhanced the removal of *E. coli* by 29.6%, as observed in the experimental results (Section 3.3). This enhancement is attributed to increased collisions between the Fe_3O_4@ZIF-8@Ag_2O magnetic nanocomposites (MNCs) and *E. coli* cells, facilitated by the magnetic field. Below, we provide a detailed mechanistic explanation, supported by theoretical considerations, including the influence of the Lorentz force and nanoparticle–bacteria interactions.

Table 3 Model parameters obtained from fitting the experimental data

Model	Chick–Watso				Weibull				
Strain	k_{max}	$Log_{10}(C_i)$	R^2	RMSE	β	δ	$Log_{10}(C_i)$	R^2	RMSE
Inactivation without magnetic field									
E. coli	0.056	5.32	0.926	0.16	0.56	26.31	5.56	0.989	0.07
Inactivation with magnetic field									
E. coli	0.092	5.36	0.962	0.18	0.92	23.04	5.56	0.963	0.21

The Fe_3O_4@ZIF-8@Ag_2O MNCs, characterized by a saturation magnetization of 30.47 emu g^{-1} (Section 3.1), are responsive to the applied 2 mT magnetic field generated by a copper solenoid coil. This field induces a magnetic force on the MNCs, which can be described by the magnetic force equation:

$$F_m = \nabla(m \times B) \quad (19)$$

where F_m is the magnetic force, m is the magnetic moment of the nanoparticle, and B is the magnetic field. For superparamagnetic Fe_3O_4-based nanoparticles, the magnetic moment aligns with the external field, causing the MNCs to experience a force toward regions of higher field strength, typically near the solenoid coils. This results in the stabilization and confinement of MNCs within the central region of the reactor, as observed in Fig. 6a, increasing the local concentration of MNCs and extending the contact time with *E. coli* cells.

Additionally, the magnetic field induces oscillatory motion in the MNCs due to field gradients and possible alternating components in the solenoid-driven field. This motion enhances the probability of collisions between MNCs and *E. coli* cells. The increased collision frequency is critical, as the MNCs, with a mean crystallite size of 30.62 nm (Section 3.1), possess a large surface area capable of penetrating bacterial cell walls upon contact, disrupting essential enzymatic functions and leading to cell inactivation.[21,57]

The *E. coli* cell membrane, composed of phospholipids and proteins, contains charged components that are susceptible to electromagnetic interactions. In the presence of a magnetic field, charged particles (*e.g.*, ions or charged groups on the membrane) experience a Lorentz force, given by

$$F_L = q(v \times B) \quad (20)$$

where F_L is the Lorentz force, q is the charge, v is the velocity of the charged particle, and B is the magnetic field. In the reactor, *E. coli* cells are in motion due to Brownian dynamics and fluid flow. The 2 mT magnetic field, though relatively weak, can exert a Lorentz force on charged membrane components, particularly divalent cations (*e.g.*, Ca^{2+} or Mg^{2+}) that stabilize the outer membrane of Gram-negative bacteria like *E. coli*. This force may induce localized membrane stress or reorientation of charged lipids, increasing membrane permeability and susceptibility to penetration by MNCs.

Furthermore, the magnetic field may influence the electrophoretic mobility of *E. coli* cells, which typically carry a negative surface charge due to lipopolysaccharides in their outer membrane. The Lorentz force could enhance the directional movement of *E. coli* toward regions of high MNC concentration, further increasing collision rates. This effect is analogous to magnetophoresis, where charged or polarizable particles migrate in a magnetic field gradient, as described by the following:

$$v_m = (\chi V/6\pi\eta r)\nabla B^2 \quad (21)$$

where v_m is the magnetophoretic velocity, χ is the magnetic susceptibility, V is the particle volume, η is the medium viscosity, r is the particle radius, and ∇B^2 is the magnetic field gradient squared. While *E. coli* cells are not inherently magnetic, their interaction with MNCs, which may adhere to the cell surface, could impart a weak magnetic susceptibility, amplifying magnetophoretic effects.

The role of the Lorentz force in enhancing nanoparticle–bacteria interactions is well supported by prior studies,[61] which demonstrated that weak to moderate static or oscillating magnetic fields promote magnetophoresis, leading to increased bacterial capture and removal efficiencies in water treatment systems containing superparamagnetic nanoparticles. The results are consistent with the observed increase in *E. coli* removal in the present work. Moreover, magnetophoresis-induced confinement of magnetic nanocomposites has been shown to enhance collision frequency and facilitate the transport of bacteria towards active nanoparticle surfaces.[62] The present results further confirm that the combined effects of the Lorentz force and magnetophoretic migration contribute significantly to bacterial deactivation in magnetically assisted reactors.

The enhanced collision frequency facilitated by the magnetic field amplifies the antibacterial mechanisms of the Fe_3O_4@ZIF-8@Ag_2O MNCs. As detailed in Section 3.3, the MNCs release ions (*e.g.*, Ag^+ from Ag_2O and Zn^{2+} from ZIF-8) that disrupt ATP production, DNA replication, and protein function. The magnetic field stimulates the generation of reactive oxygen species (ROS) by Fe_3O_4 and Ag_2O nanoparticles, as electrons are captured at active sites and react with dissolved oxygen to form ROS, such as superoxide (O_2^-) or hydroxyl radicals ($OH^\bullet$). The increased collision rate ensures that these ROS are delivered more effectively to the bacterial cell surface, exacerbating oxidative stress and lipid damage.

Moreover, the physical penetration of MNCs into the *E. coli* cell wall, facilitated by their large surface area, is enhanced under magnetic field conditions. The field-driven oscillatory motion of MNCs increases the likelihood of mechanical disruption of the cell wall, allowing ions and ROS to access intracellular targets more readily. This synergistic effect, combining physical penetration, ion release, and ROS generation, underpins the observed 29.6% increase in *E. coli* removal, with removal rates reaching 99.83% at 60-minutes under magnetic field conditions (Fig. 6c).

The kinetic modeling results (Section 3.4) further corroborate the mechanistic role of the magnetic field. The Chick–Watson model shows an increased rate constant (k_{max} = 0.092 min^{-1}) under magnetic field conditions compared to without (k_{max} = 0.056 min^{-1}), indicating a faster inactivation rate driven by enhanced nanoparticle–bacteria interactions. The Weibull model's shape parameter (β) increases from 0.56 to 0.92 with the magnetic field, suggesting a more pronounced initial inactivation phase, consistent with increased collision frequency and membrane disruption early in the process.

In summary, the 2 mT magnetic field enhances *E. coli* removal by increasing the collision frequency between Fe_3O_4@ZIF-8@Ag_2O MNCs and bacterial cells through magnetic force-induced nanoparticle confinement and oscillatory motion. The Lorentz force on charged membrane components increases membrane susceptibility, while synergistic antibacterial mechanisms of ion release, ROS generation, and physical penetration are amplified by the

field. These interactions collectively account for the observed 29.6% enhancement in removal efficiency, providing a robust theoretical framework for the experimental findings.

4. Conclusion

This study utilized a magnetically assisted reactor for the removal of *E. coli* from aqueous systems. To optimize the bacterial removal efficiency, a reactor incorporating novel design parameters was developed. A primary objective was to maintain thermal stability throughout the experiment, thereby preserving *E. coli* viability. Additionally, to isolate the specific contributions of the magnetic field and nanoparticles to bacterial removal, the solenoid wire coil was engineered to minimize heat generation. Following the reactor design, *E. coli*-contaminated water, prepared by suspending the bacterial strain in a distilled water-PBS solution, was introduced as the influent. Experimental findings indicate that bacterial survival is prolonged in PBS compared to pure water. Furthermore, the study demonstrates that MNPs, due to their high surface area, significantly enhance the removal efficiency of *E. coli* within the reactor. The applied magnetic field stabilizes the nanoparticles, thereby increasing their interaction with bacterial cells and further improving removal efficiency. The experimental results were validated by fitting the data to the Chick–Watson and Weibull kinetic models, both of which demonstrated a high degree of accuracy in predicting bacterial inactivation. To achieve the experimental objectives, a solenoid wire coil was utilized to generate a 2 mT magnetic field surrounding the reactor, thereby enhancing *E. coli* removal efficiency. Under the influence of the magnetic field, the bacterial removal efficiency increased by 29.6% in 60-minutes. This enhancement is attributed to the increased collision between *E. coli* and nanoparticles. Consequently, a maximum removal rate of 99.83% was achieved within the same duration. The Weibull model, in the absence of a magnetic field, exhibited a coefficient of determination (R^2) of 0.9896 and the lowest RMSE of 7%. In conclusion, the synergistic application of MNCs and external magnetic fields significantly enhances bacterial removal from aqueous solutions, offering a rapid and highly efficient disinfection approach.

Abbreviation

A	Ampere
B	Magnetic field (mT)
C	Concentration (CFU mL^{-1})
D	Diameter (m)
d	Distance between the lattice planes (nm)
h	Convective heat transfer coefficient (W m^{-2} k^{-1})
I	Electric current (A)
k	Thermal conductivity (W m^{-1} K^{-1})
L	Length (m)
N	Number of wire turns
n	Positive integer
P	Electric power (W)
Q	Energy (J)
$\dot{q}$	Heat rate generated (W m^{-3})
R	Resistance of the wire (Ω)
r	Radius (m)
t	Time (min)
V	Volts
W	Watt
X	Crystallite size (nm)
β	Shape factor (–)
ρ	Resistivity (Ω m)
δ	First decimal reduction time (min)
μ	Vacuum permeability (N A^{-2})
λ	X-ray wavelength (nm)
con	Consumption
cum	Cumulative
e	Effluent
exp	Experimental
gen	Generated
i	Influent
in	Input
max	Maximum
np	Nanoparticle
out	Output
pre	Predicted
s	Surface
ATP	Adenosine triphosphate
CFU	Colony form unit
DC	Direct current
DNA	Deoxyribonucleic acid
EDX	Energy-dispersive X-ray
FCC	Face-centered cubic
FWHM	Full width at half maximum (radians)
mT	Millitesla
PBS	Phosphate-buffered saline
RMSE	Root mean square error
R%	Removal percentage
SEM	Scanning electron microscopy
VSM	Vibrating-sample magnetometer
XRD	X-ray diffraction

Data availability

Data are available from the authors upon request.

Conflicts of interest

There are no known conflicts of interest to declare.

Acknowledgements

This research was conducted in the laboratory of the Faculty of Chemistry at the University of Tabriz. The authors express their sincere gratitude to Prof. Hemayat Shekaari for his generous provision of laboratory equipment and support.

References

1 V. Saxena, *Water, Air, Soil Pollut.*, 2025, **236**, 1–40.
2 T. A. Tella, B. Festus, T. D. Olaoluwa and A. S. Oladapo, *Smart Nanomaterials for Environmental Applications*, 2025, pp. 351–385.

3 B. Golmohammadi and H. Shekaari, *Ultrason. Sonochem.*, 2024, **108**, 106974.
4 H. Shekaari and B. Golmohammadi, *Ultrason. Sonochem.*, 2021, **74**, 105549.
5 B. Golmohammadi, H. Shekaari, A. Rostami and A. Olad, *Desalination*, 2024, **587**, 117911.
6 M. Hermani, B. Golmohammadi and H. Shekaari, *RSC Adv.*, 2024, **14**, 24352–24364.
7 S. Nickabadi, B. Golmohammadi and H. Rostami, *J. Environ. Chem. Eng.*, 2025, **13**, 115975.
8 S. Nickabadi, B. Golmohammadi and M. Hadavi, *Sci. Rep.*, 2025, **15**(1), 1–17.
9 J. Zhang, R. Cao, W. Song, L. Liu and J. Li, *J. Colloid Interface Sci.*, 2022, **607**, 1730–1740.
10 Q. Li, C. Yong, W. Cao, X. Wang, L. Wang, J. Zhou and X. Xing, *J. Colloid Interface Sci.*, 2018, **511**, 285–295.
11 Z. Zhu, C. Huang, L. Liu, J. Wang and X. Gou, *J. Colloid Interface Sci.*, 2024, **661**, 374–388.
12 S. Lin, D. Lu and Z. Liu, *Chem. Eng. J.*, 2012, **211–212**, 46–52.
13 R. Han, W. Zou, H. Li, Y. Li and J. Shi, *J. Hazard. Mater.*, 2006, **137**, 934–942.
14 O. F. González Vázquez, M. d R. Moreno Virgen, V. Hernandez Montoya, R. Tovar Gomez, J. L. Alcantara Flores, M. A. Pérez Cruz and M. A. Montes Morán, *Ind. Eng. Chem. Res.*, 2016, **55**, 9323–9331.
15 S. M. Sosa, R. Huertas and V. J. Pereira, *Membranes*, 2023, **13**, 56.
16 I. Neme, G. Gonfa and C. Masi, *Case Stud. Chem. Environ. Eng.*, 2023, **7**, 100320.
17 N. Fitriani, P. E. Ardiyanti, E. P. Kuncoro, W. D. Budiyanto, D. R. M. Isnadina, F. E. Wahyudianto and R. M. S. R. Mohamed, *Heliyon*, 2020, **6**(4), e03736.
18 S. Rathinavelu, G. Divyapriya, A. Joseph, I. M. Nambi, A. B. Muthukrishnan and G. Jayaraman, *Environ. Res.*, 2022, **210**, 112749.
19 N. Y. Rachel, B. Abdelaziz, N. J. Nsami, K. Daouda, Y. Abdelrani, L. Mehdi, L. Khalid and K. M. Joseph, *Int. J. Adv. Chem.*, 2018, **6**, 46.
20 M. Pinto, P. S. F. Ramalho, N. F. F. Moreira, A. G. Gonçalves, O. C. Nunes, M. F. R. Pereira and O. Soares, *Environ. Adv.*, 2020, **2**, 100010.
21 L. Wang, C. Hu and L. Shao, *Int. J. Nanomed.*, 2017, 1227–1249.
22 L. Akhigbe, S. Ouki and D. Saroj, *Chem. Eng. J.*, 2016, **295**, 92–98.
23 N. Ebrahimi, P. Schimpf and A. Jafari, *Sens. Actuators, A*, 2018, **284**, 276–285.
24 A. Malvandi and D. D. Ganji, *J. Magn. Magn. Mater.*, 2014, **362**, 172–179.
25 L. Lipus, A. Hamler, B. Buchmeister and A. Gorsek, *DAAAM Int. Sci. Book*, 2018, **9**, 97–106.
26 M. Łebkowska, A. Rutkowska-Narożniak, E. Pajor, A. Tabernacka and M. Załęska-Radziwiłł, *Environ. Sci. Pollut. Res.*, 2018, **25**, 22571–22583.
27 R. Selamat, I. Abustan, M. R. Arshad and N. H. M. Kamal, *Water and Wastewater Treatment*, 2019.
28 K. K. Donovan, G. T. Fermin, I. Vigil, S. Shaker, R. A. Paulino, R. Difo and Y. Ye, *Front. Chem. React. Eng.*, 2025, **7**, 1565754.
29 S. Gajbhiye and S. Sakharwade, *Dermatol. Sci. Appl.*, 2016, **6**(1), 48–53.
30 S. Kampe, R. Kaegi, K. Schlich, C. Wasmuth, H. Hollert and C. Schlechtriem, *Environ. Toxicol. Chem.*, 2018, **37**(6), 1606–1613.
31 S. Khan, M. Zahoor, R. S. Khan, M. Ikram and N. U. Islam, *Heliyon*, 2023, **9**(6), e16928.
32 Z. Mat Lazim, S. Salmiati, M. Marpongahtun, N. Z. Arman, M. R. Mohd Haniffah, S. Azman, E. L. Yong and M. R. Salim, *Water*, 2023, **15**(7), 1349.
33 S. Pakrashi, C. Tan and W. X. Wang, *Environ. Toxicol. Chem.*, 2017, **36**(12), 3359–3366.
34 P. M. Potter, J. Navratilova, K. R. Rogers and S. R. Al-Abed, *Environ. Sci.: Nano*, 2019, **6**(2), 592–598.
35 C. Sun, K. Hu, D. Mu, Z. Wang and X. Yu, *Microorganisms*, 2022, **10**(10), 2080.
36 Q. Wu, D. Wang, C. Chen, C. Peng, D. Cai and Z. Wu, *J. Environ. Manage.*, 2021, **290**, 112626.
37 K. Maesaroh, M. D. Permana, D. R. Eddy and I. Rahayu, *Trends Sci.*, 2023, **20**, 4350.
38 Y. Pan, Y. Liu, G. Zeng, L. Zhao and Z. Lai, *Chem. Commun.*, 2011, **47**, 2071–2073.
39 X. Tang, W. Zeng, C. Wang, F. Pan, J. Wei and L. Wu, *Chem. Eng. J.*, 2025, **508**, 161149.
40 Y. Jin, J. Deng, J. Liang, C. Shan and M. Tong, *Colloids Surf., B*, 2015, **136**, 659–665.
41 F. M. Alzahrani, N. S. Alsaiari, K. M. Katubi, A. Amari, F. Ben Rebah and M. A. Tahoon, *Polymers*, 2021, **13**(11), 1742.
42 M. Bilal, H. M. Iqbal, S. F. Adil, M. R. Shaik, A. Abdelgawad, M. R. Hatshan and M. Khan, *J. Adv. Res.*, 2022, **38**, 157–177.
43 K. Yildirim, C. Atas, E. Simsek and A. Y. Coban, *Microbiol. Spectrum*, 2023, **11**, e00319–e00323.
44 H. E. Watson, *Epidemiol. Infect.*, 1908, **8**, 536–542.
45 A. H. Geeraerd, V. P. Valdramidis and J. F. Van Impe, *Int. J. Food Microbiol.*, 2005, **102**, 95–105.
46 A. C. Mecha, M. S. Onyango, A. Ochieng and M. N. B. Momba, *Environ. Eng. Res.*, 2020, **25**, 890–897.
47 P. Guan, S. O. Prasher, M. T. Afzal, S. George, J. Ronholm, J. Dhiman and R. M. Patel, *Ecol. Eng.*, 2020, **150**, 105819.
48 Y. Huang, Y. Lu, R. Huang, J. Chen, F. Chen, Z. Liu, X. Yu and A. P. Roskilly, *Energy Procedia*, 2017, **142**, 4029–4036.
49 F. P. Incropera, D. P. DeWitt, T. L. Bergman and A. S. Lavine, *Fundamentals of Heat and Mass Transfer*, Wiley, New York, 1996, vol. 6.
50 F. X. Hart, *Phys. Teach.*, 2018, **56**, 104–106.
51 R. Bakhshali-Dehkordi and M. A. Ghasemzadeh, *J. Mol. Struct.*, 2021, **1236**, 130298.
52 C. Shan, Z. Su, Z. Liu, R. Xu, J. Wen, G. Hu, T. Tang, Z. Fang, L. Jiang and M. Li, *Molecules*, 2023, **28**, 4155.
53 H. Kaur, G. C. Mohanta, V. Gupta, D. Kukkar and S. Tyagi, *J. Drug Delivery Sci. Technol.*, 2017, **41**, 106–112.
54 S. Nasiri, M. Rabiei, A. Palevicius, G. Janusas, A. Vilkauskas, V. Nutalapati and A. Monshi, *NanoTrends*, 2023, **3**, 100015.
55 H. Nadimi, H. Sarpoolaky and M. Soltanieh, *Ceram. Int.*, 2021, **47**, 12859–12869.

56 W. Lai, J. Zhang, J. Sun, T. Min, Y. Bai, J. He, H. Cao, Q. Che, J. Guo and Z. Su, *Int. J. Biol. Macromol.*, 2024, **278**, 134809.
57 Z. Xu, C. Zhang, X. Wang and D. Liu, *ACS Appl. Bio Mater.*, 2021, **4**, 3985–3999.
58 Y. Nakamura, K. Okita, D. Kudo, D. N. D. Phuong, Y. Iwamoto, Y. Yoshioka, W. Ariyoshi and R. Yamasaki, *Nanomaterials*, 2021, **11**, 1584.
59 R. Chaudhary, N. Singh, G. Nagpal and F. K. Saah, *Microbe*, 2024, **5**, 100221.
60 M.-Y. Alikhani, S.-M. Lee, J.-K. Yang, M. Shirzad-Siboni, H. Peeri-Dogaheh, M.-S. Khorasani, M.-A. Nooshak and M.-R. Samarghandi, *Water Sci. Technol.*, 2013, **67**(3), 557–563.
61 Y. Ji, S. Gao, R. Si, Z. Zhang, L. Tian, W. Guan and T. Zhang, *Geochim. Cosmochim. Acta*, 2023, **349**, 115–125.
62 S. S. Leong, Z. Ahmad, S. C. Low, J. Camacho, J. Faraudo and J. Lim, *Langmuir*, 2020, **36**(28), 8033–8055.